Journal of Porphyrins and Phthalocyanines
J. Porphyrins Phthalocyanines 2020; **24**: 286–297
DOI: 10.1142/S1088424619500822

Published at https://www.worldscinet.com/jpp/

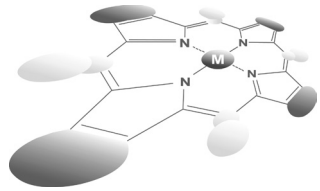

Synthesis and optical, magnetic, and electrochemical properties of 5,10,15,20-tetraaryl-5,15-diazaporphyrin — tertiary amine conjugates

Keisuke Sudoh[a], Yuna Satoh[b], Ko Furukawa[c], Haruyuki Nakano[d] and Yoshihiro Matano*[,b◊]

[a]*Department of Fundamental Sciences, Graduate School of Science and Technology, Niigata University, Nishi-ku, Niigata 950-2181, Japan*
[b]*Department of Chemistry, Faculty of Science, Niigata University, Nishi-ku, Niigata 950-2181, Japan*
[c]*Center for Coordination of Research Facilities, Institute for Research Promotion, Niigata University, Nishi-ku, Niigata 950–2181, Japan*
[d]*Department of Chemistry, Graduate School of Science, Kyushu University, Fukuoka 819-0395, Japan*

Dedicated to Professor Atsuhiro Osuka on the occasion of his 65th birthday.

Received 12 June 2019
Accepted 1 July 2019

ABSTRACT: We report on the synthesis and optical, magnetic, and electrochemical properties of nickel(II) and copper(II) complexes of 5,10,15,20-tetraaryl-5,15-diazaporphyrin–tertiary amine (TADAP–TA) conjugates. Metal-templated cyclization reactions of 9-(4-(dimethylamino)phenyl)amino-1-chloro-5-mesityldipyrrin and 9-(4-(diphenylamino)phenyl)amino-1-chloro-5-mesityldipyrrin (mesityl = 2,4,6-trimethylphenyl) with nickel(II) or copper(II) acetate afforded the corresponding metal(II) complexes of TADAP–TA. The 20π, 19π, and 18π oxidation states of the DAP ring in the TADAP–TAs were reversibly interconvertible by redox reactions. NMR spectroscopy of the 20π and 18π Ni-TADAP–TAs revealed their antiaromatic and aromatic characters, respectively, whereas electron paramagnetic resonance spectroscopy of the 19π Ni-TADAP–TAs showed effective delocalization of an unshared electron spin in the DAP ring. The interconversion between the three oxidation states of TADAP–TAs also caused a distinct change in the optical properties of the DAP π-electron system. Notably, all the 18π dications exhibited weak and broad absorption bands in the near infrared region owing to the charge-transfer from the peripheral tertiary amine units (donor) to the cationic DAP center (acceptor). Cyclic voltammetry of TADAP–TAs exhibited the reversible 20π/19π and 19π/18π redox couples and the irreversible amine oxidation at the periphery. The electrochemical oxidation of the Ni-TADAP–triphenylamine conjugate generated reactive ammoniumyl radicals, which underwent intermolecular coupling to form a polymer of TADAP–TA on the electrode surface.

KEYWORDS: aromaticity, charge–transfer interaction, diazaporphyrin, radical, redox property.

INTRODUCTION

5,15-Diazaporphyrin (DAP) and its derivatives have drawn considerable attention because of their characteristic optical and electrochemical properties. DAPs have large molar absorptivities in the long-wavelength region, and the highest occupied molecular orbital (HOMO) and lowest unoccupied molecular orbital (LUMO) of DAPs are low-lying compared with those of porphyrin analogs [1–5]. These physical properties of DAPs can be finely tuned by various substituents at the periphery [6–14]. For example, the electron-rich substituents such as amino and *para*-aminophenyl

◊ SPP full member in good standing.

*Correspondence to: Yoshihiro Matano, Department of Chemistry, Faculty of Science, Niigata University, Nishi-ku, Niigata 950-2181, Japan; tel.: +81-25-262-7734; fax: +81-25-262-7734; email: matano@chem.sc.niigata-u.ac.jp.

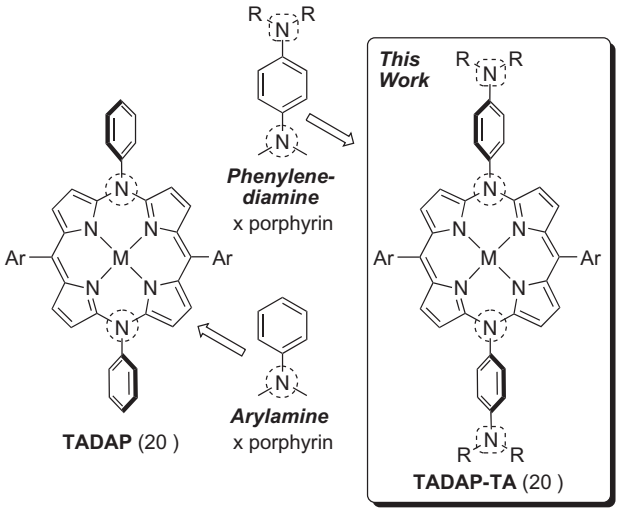

Chart 1. TADAP and TADAP–TA. (Ar = 2,4,6-$Me_3C_6H_2$; *R* = Me or Ph in this work)

groups provide a large charge-transfer (CT) character to DAP chromophores when attached at peripheral pyrrolic β-positions [6–12]. Furthermore, the resulting donor–acceptor-type DAP dyes have been applied in dye-sensitized solar cells [11] and photodynamic destruction of cancer cells [12]. Recently, we have developed a convenient method for the synthesis of *meso-N*-functionalized DAPs, 5,10,15,20-tetraaryl-5,15-diazaporphyrins (TADAPs) and their derivatives [15–19]. From a structural viewpoint, TADAP is regarded as a hybrid of porphyrin and arylamines (Chart 1, left) having two more π-electrons than 5,10,15,20-tetraarylporphyrin (TAP). This hybridization alters the net charge of the TAP π-circuits of two electrons; the 20π, 19π, and 18π TADAPs are present in neutral form, cation, and dication, respectively, whereas the isoelectronic TAPs are present in dianion, anion, and neutral form. This alteration of the charge provides remarkable stability, particularly to the 20π and 19π oxidation states of the DAP π-electron system. To further explore the variation in redox properties of DAP π-electron systems, we envisioned that fusion of a porphyrin ring with *p*-phenylenediamines might provide TADAP–tertiary amine (TADAP–TA) conjugates as a new platform for redox-switchable porphyrinoid materials (Chart 1, right). Herein, we report the first examples of nickel(II) and copper(II) complexes of TADAP-TAs, which have *N*,*N*-dimethylaniline or triphenylamine units on the *meso*-N atoms of a DAP ring. Our research aim was to reveal the influence of the

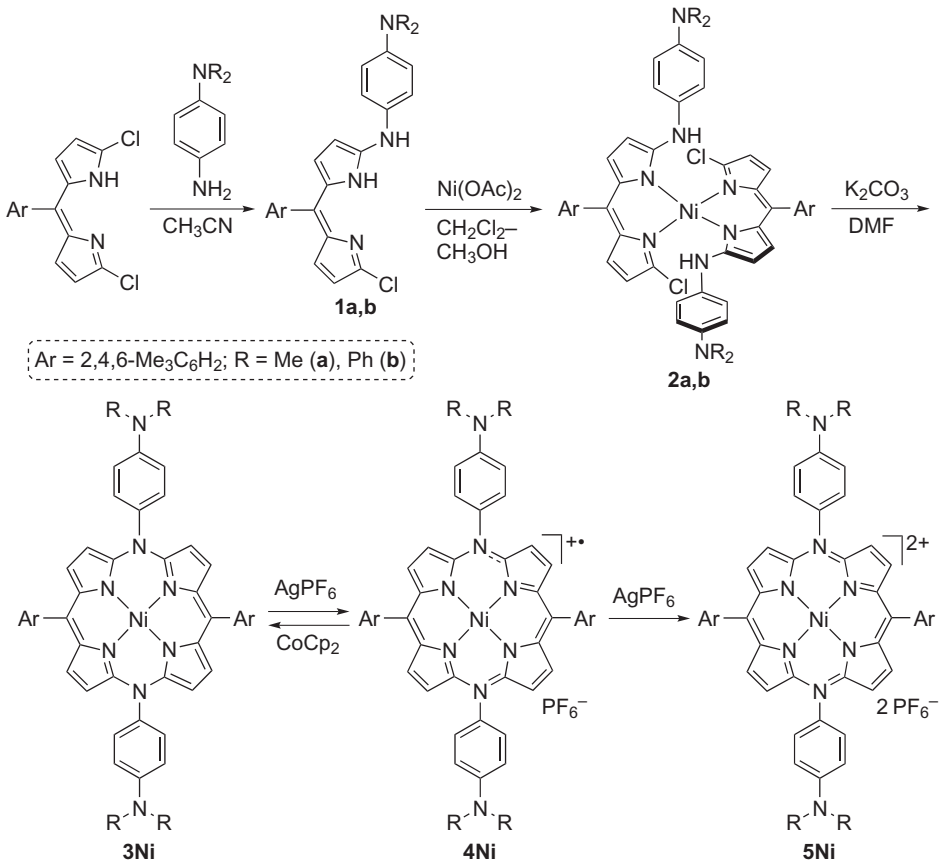

Scheme 1. Synthesis of **1**, **2**, **3Ni**, **4Ni**, and **5Ni**

peripheral tertiary amine units on the optical, magnetic, and electrochemical properties of the DAP π-electron systems. The electrochemical behavior of the TADAP–triphenylamine conjugate was also investigated using cyclic voltammetry.

RESULTS AND DISCUSSION

First, we synthesized nickel(II) complexes (Ni-TADAP-TAs) according to the previously reported methodologies (Scheme 1) [14, 15]. Treatment of 9-(4-(dimethylamino) phenyl)amino-1-chloro-5-mesityldipyrrin **1a** and 9-(4-(diphenylamino)phenyl)amino-1-chloro-5-mesityldipyrrin **1b** (mesityl = 2,4,6-trimethylphenyl), which were obtained from 1,9-dichloro-5-mesityldipyrrin [20] and the corresponding 1,4-phenylenediamine derivatives, with a half equivalent of nickel(II) acetate in CH_2Cl_2–MeOH gave nickel(II)–bis(dipyrrin) complexes **2a** and **2b**, respectively. Metal-templated cyclization of **2a**,**b** proceeded in the presence of K_2CO_3 in *N*,*N*-dimethylformamide (DMF) at 110 °C to afford the 20π Ni-TADAP–TAs **3Ni-a**,**b**, which were isolated as reddish-brown solids by recrystallization from CH_2Cl_2–MeOH. Oxidation of **3Ni-a**,**b** with one equivalent of silver(I) hexafluorophosphate ($AgPF_6$) afforded the 19π radical cations **4Ni-a**,**b**, and further oxidation of **4Ni-a**,**b** with one additional equivalent of $AgPF_6$ gave the 18π dications **5Ni-a**,**b**. Reduction of **4Ni-a**,**b** with bis(cyclopentadienyl)cobalt(II) (Cp_2Co) in THF smoothly took place to give **3Ni-a,b**.

Next, we synthesized copper(II) complexes of TADAP–TA (Cu-TADAP–TAs) (Scheme 2). The reaction of **1a** with one equivalent of copper(II) acetate took place at room temperature to afford the 19π Cu-TADAP–TA **4Cu-a** *via* successive metal complexation, metal-templated cyclization, and single-electron oxidation (from

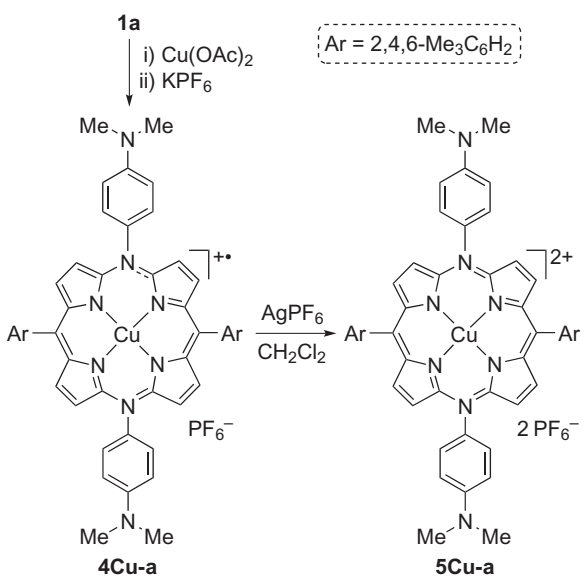

Scheme 2. Synthesis of **4Cu** and **5Cu**

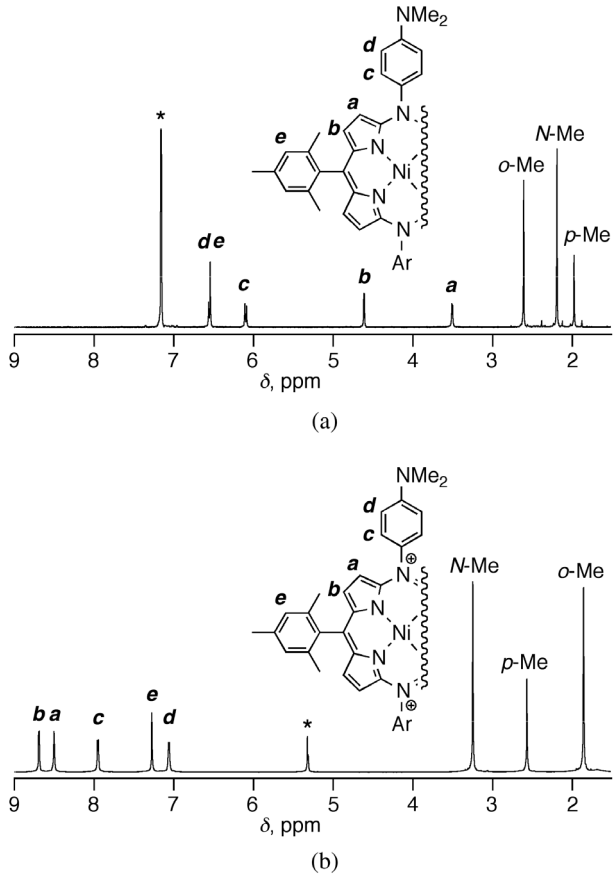

Fig. 1. ^{1}H NMR spectra (δ 1.5–9.0 ppm) of (a) **3Ni-a** in C_6D_6 and (b) **5Ni-a** in CD_2Cl_2. Asterisks indicate residual solvent peaks

20π to 19π) steps. This type of one-pot multi-step reaction has been typically observed for the synthesis of the copper(II) complexes of TADAP and related macrocycles [16, 19]. Reaction of **4Cu-a** with $AgPF_6$ afforded the 18π dications **5Cu-a**. Attempts to isolate a 20π Cu-TADAP–TA in pure form have so far been unsuccessful because it is easily re-oxidized to the parent 19π species in solution (see, Experimental section).

The newly prepared TADAP–TAs were characterized by ^{1}H and ^{13}C NMR spectroscopy, IR spectroscopy, and high-resolution mass spectrometry (HRMS). In the HRMS spectra, molecular ion peaks ($[M]^+$) were observed for **3Ni**, whereas fragment ion peaks consistent with m/z = $[M-PF_6]^+$ and $[M-2(PF_6)]^{z+}$ (z = 1, 2) were detected for **4M** and **5M**, respectively. In the IR spectra of radical cations **4M** and dications **5M**, the P–F stretching vibration mode of the hexafluorophosphate ion was observed at ν_{max} = 830–835 cm^{-1}. As illustrated in Fig. 1, the ^{1}H NMR spectra of the *para*-Me_2N-substituted derivatives **3Ni-a** and **5Ni-a** showed their peripheral pyrrolic β-protons at δ 3.50/4.61 ppm (in C_6D_6) and δ 8.51/8.67 ppm (in CD_2Cl_2), respectively. These spectral features clearly show the antiaromatic and aromatic character of the DAP macrocyclic π-electron systems

in **3Ni-a** and **5Ni-a**, respectively. In the case of **5Ni-a**, the inductive effect derived from the positive charge of the DAP ring also contributed to the appearance of its *meso*-aryl groups in the downfield region. The *para*-Ph_2N-substituted derivatives **3Ni-b** and **5Ni-b** exhibited similar paratropic and diatropic ring-current effects, respectively, in their ^{1}H NMR spectra; *i.e.* the peripheral pyrrolic β-protons were observed at δ 3.50/4.66 ppm for **3Ni-b** (in C_6D_6) and δ 8.61/8.77 ppm for **5Ni-b** (in CD_2Cl_2).

As shown in Figs 2a, 2b, **4Ni-a** and **4Ni-b** in CH_2Cl_2 exhibited electron paramagnetic resonance (EPR) signals with similar splitting patterns at g = 1.998. The simulated spectra indicated that the observed hyperfine structures were mainly attributed to two ^{14}N and four ^{1}H nuclei. The calculated structures and spin densities of 19π Ni-TADAP–TA models **4Ni-am** and **4Ni-bm**, in which the *meso*-mesityl groups were replaced by phenyl groups, indicated that the unshared electron spin was not distributed onto the peripheral tertiary amine moieties but delocalized over the entire DAP ring in each radical cation (Figs 2c, 2d). The poor π-orbital overlap between the *meso*-aryl and DAP rings, which intersect perpendicularly, likely disturbed the effective resonance interactions between these rings. Therefore, in the 19π radical cations **4Ni-a** and **4Ni-b**, the two *meso*-N and four β–H atoms make a considerable contribution to the hyperfine coupling, whereas the peripheral tertiary amine units make little contribution to the spin distribution.

The ultraviolet/visible/near infrared (UV/vis/NIR) absorption spectra of **3Ni**, **4M**, and **5M** in CH_2Cl_2 are shown in Fig. 3, and the experimentally observed optical data are summarized in Table 1. The change of the central metal from nickel(II) to copper(II) exerted little effect on the absorption maximum (λ_{max}) values. All the TADAP–TAs exhibited intense absorption bands in the

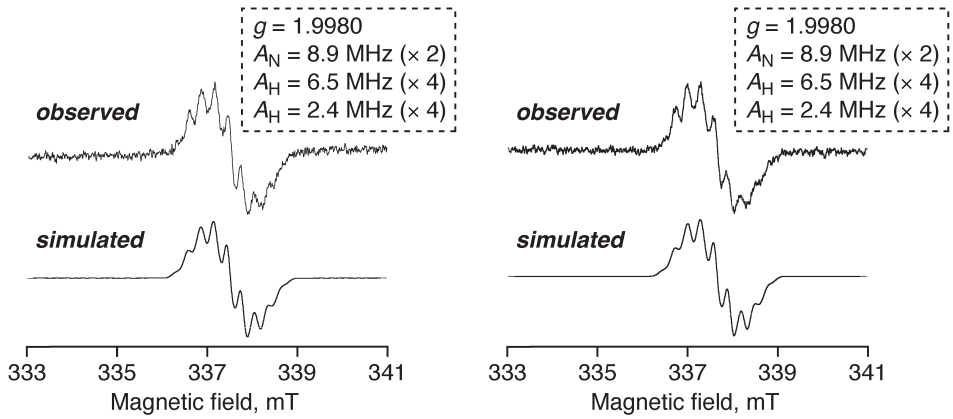

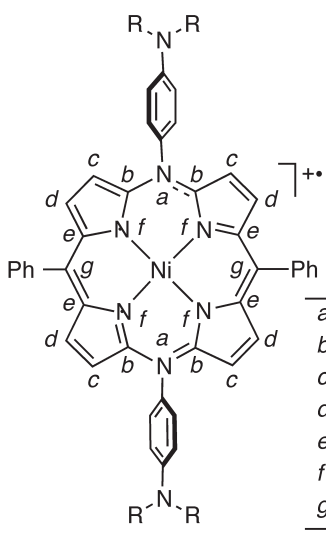

	4Ni-am R = Me	4Ni-bm R = Ph
a	0.139	0.137
b	0.026	0.026
c	0.085	0.083
d	0.022	0.021
e	0.146	0.145
f	0.011	0.011
g	0.091	0.091

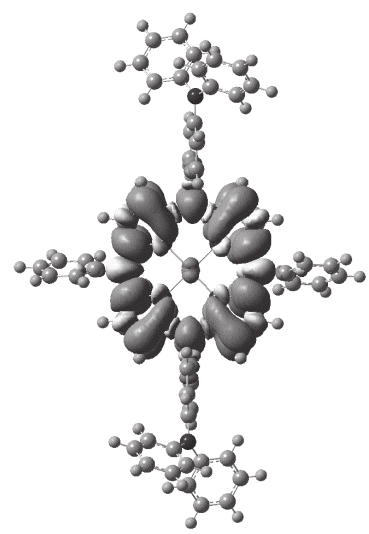

Fig. 2. EPR spectra of (a) **4Ni-a** and (b) **4Ni-b**: observed in CH_2Cl_2 at 298 K (upper) and simulated (lower). (c) Spin densities at the DAP ring of **4Ni-am** and **4Ni-bm**; calculated by the DFT method with the solvent effect (PCM, CH_2Cl_2). (d) Spin density distribution at the optimized structure of **4Ni-bm**

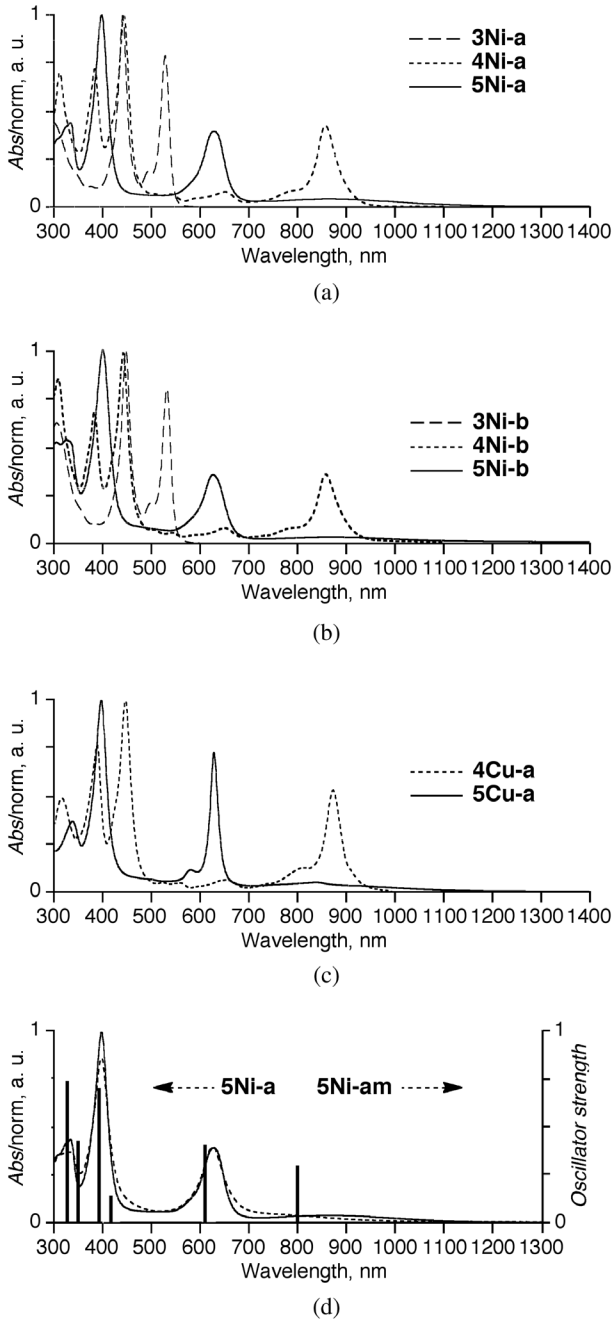

Fig. 3. UV/vis/NIR absorption spectra of (a) **3Ni-a** (dashed line), **4Ni-a** (dotted line), and **5Ni-a** (solid line), (b) **3Ni-b** (dashed line), **4Ni-b** (dotted line), and **5Ni-b** (solid line), and (c) **4Cu-a** (dotted line) and **5Cu-a** (solid line) in CH_2Cl_2. (d) UV/vis/NIR absorption spectra of **5Ni-a** in CH_2Cl_2 (solid line) and in toluene (dotted line) and TD-DFT excitations of **5Ni-am** (bar graphs) including the solvent effect (PCM, CH_2Cl_2)

higher-energy visible region (390–450 nm) and additional characteristic bands in the lower-energy visible and NIR regions. The spectral features of **3Ni**, **4M**, and **5M** were in good accordance with those previously reported for TADAP derivatives [15, 16], highlighting the redox-switchable optical properties of the TADAP π-electron systems. Notably, the 18π dications **5M** showed additional broad absorption bands in the NIR region (700–1200 nm). The related 18π TADAP dications bearing *p*-anisyl, *p*-(*t*-butyl)phenyl, phenyl, and *p*-(trifluoromethyl)phenyl groups on the *meso*-N atoms do not show any NIR bands. These results suggest that the NIR bands of **5M** were caused by electronic excitations from the molecular orbitals that consisted of the peripheral tertiary amine units.

To gain a deeper insight into the molecular structures and the intrinsic nature of electronic excitations of the 18π dications, we performed density functional theory (DFT) calculations on models **5Ni-m** and **3Ni-m** (Fig. 4 and Table 2). In these models, the *meso*-mesityl groups were replaced by phenyl groups, and the counter anions were omitted. There are three points concerning the molecular structures that need to be addressed here. First, in both **3Ni-m** and **5Ni-m**, the bond lengths between the *meso*-N and α-C atoms are considerably shorter than those between the *meso*-N and *ipso*-C atoms, revealing that the *p* orbitals of the *meso*-N atoms were more effectively conjugated with the π-orbitals in the adjacent pyrrolic α–C atoms than those in the *ipso*-C atoms. This is because of the orientation of the *meso*-N-phenyl rings that are perpendicular to the DAP π-plane. Second, the average bond length between the *meso*-N and α–C atoms in **5Ni-m** is shorter than that in **3Ni-m** by 0.027 Å. This bond-shortening indicates that the two-electron oxidation of the DAP ring strengthens the resonance interaction between the *meso*-N and α–C atoms. Third, the bond length between the *para*-N and *ipso*-C(phenylene) atoms in **5Ni-am** (1.363 Å) is appreciably shorter than that in **3Ni-am** (1.377 Å). This result is also true for the *N*-phenyl models, **5Ni-bm** (1.392 Å) *vs*. **3Ni-bm** (1.412 Å). These data suggest that the two-electron oxidation of the DAP ring also increased the positive mesomeric effects of the *para*-R_2N groups (R = Me, Ph).

In **3Ni-m**, the HOMO (b_{3g} type) is energetically destabilized compared with the HOMO−3 (a_u type) because the HOMO includes *p*-orbitals of the *meso*-N atoms (Figs 4a, 4c). In addition to these DAP-derived MOs, the amine-centered MOs were calculated as the degenerate HOMO−1 and HOMO−2, reflecting the highly electron-donating nature of the tertiary amine units. The nature of the HOMO of TADAP–TAs varies on removal of two π-electrons from the DAP ring. In **5Ni-m**, the degenerate, amine-centered HOMO and HOMO−1 are energetically destabilized compared with the DAP-derived HOMO−2 (Figs 4b, 4d). On the basis of time-dependent DFT (TD-DFT) calculations for **5Ni-m**, we attribute the weak NIR bands observed for **5Ni** to electronic excitation from the HOMO to the LUMO (Table 2 and Fig. 3d); the oscillator strengths of these transitions are relatively small (f = 0.267–0.296). The broad NIR bands of **5Ni-a** and **5Cu-a** disappeared when an excess amount of trifluoroacetic acid was added to their CH_2Cl_2 solutions. Under acidic conditions, the

Table 1. Optical and electrochemical data for TADAPs **3Ni**, **4M**, **5M**, and **8**

	λ, nm[a]	*E*, V[b]
3Ni-a	448 (4.86), 534 (4.75)	
4Ni-a	384 (4.54), 444 (4.67), 858 (4.31)	–0.69,[c] +0.02,[c] +0.84[d]
5Ni-a	397 (4.90), 629 (4.50), 860 (3.35)	
3Ni-b	448 (4.84), 533 (4.74)	
4Ni-b	385 (4.70), 444 (4.86), 861 (4.41)	–0.64,[c] +0.03,[c] +0.77[d]
5Ni-b	400 (5.03), 626 (4.57), 863 (3.49)	
4Cu-a	387 (4.76), 445 (4.88), 867 (4.50)	–0.71,[c] –0.01,[c] +0.88[d]
5Cu-a	396 (4.86), 629 (4.72), 870 (3.43)	
8	447 (4.93), 532 (4.83)	–0.63,[c] +0.06,[c] +0.76[d]

[a] Measured in CH_2Cl_2. Absorption maxima in the range of >350 nm. Data in parentheses are logarithms of extinction coefficients. [b] Measured in CH_2Cl_2 with Bu_4NPF_6. [c] Reversible processes: The half-wave potentials ($E_{1/2}$) *vs*. Fc/Fc^+ (+0.47 V *vs*. Ag/Ag^+). [d] Irreversible processes: The oxidation potentials (E_{ox}) *vs*. Fc/Fc^+, determined by DPV.

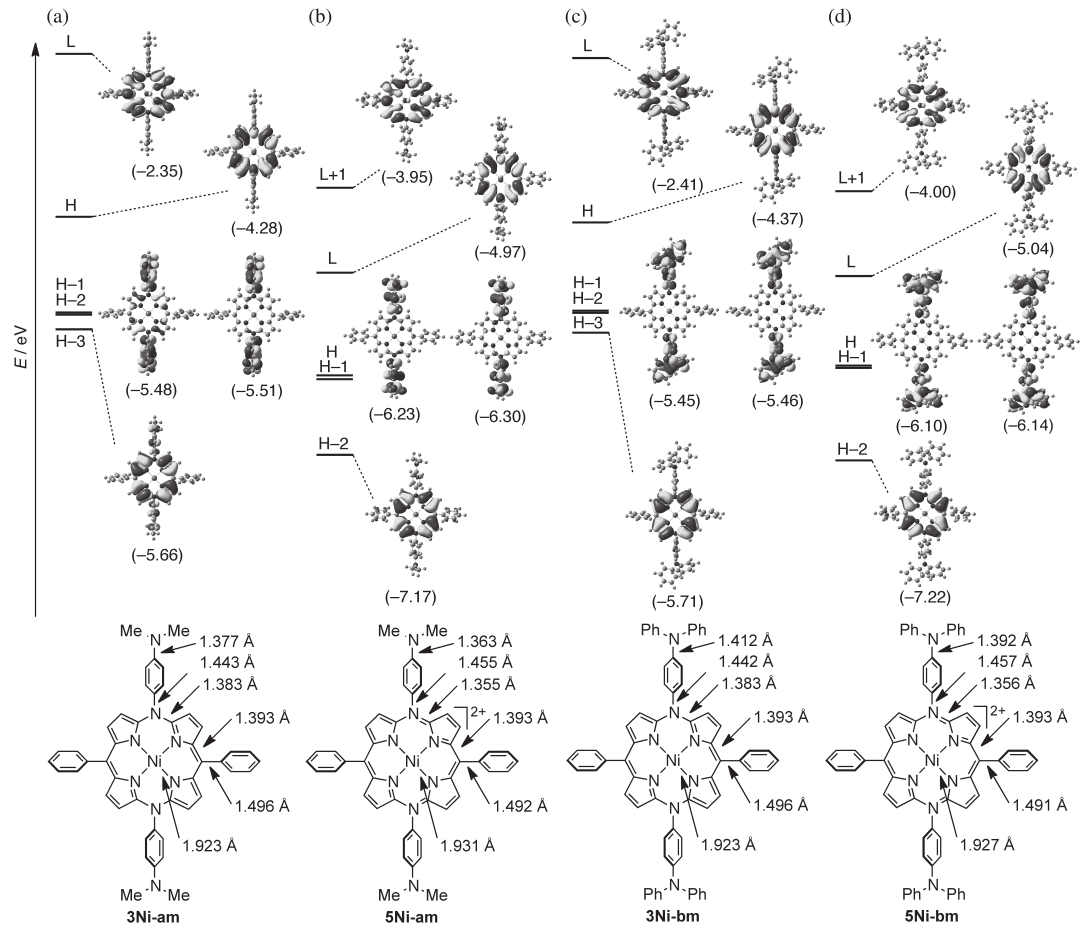

Fig. 4. Selected Kohn-Sham orbitals and their energies (in eV) of (a) **3Ni-am**, (b) **5Ni-am**, (c) **3Ni-bm**, and (d) **5Ni-bm** calculated by the DFT method with the solvent effect (PCM, CH_2Cl_2). H = HOMO; L = LUMO. Selected bond lengths (average values) are listed at the bottom

Table 2. Excitation energies and oscillator strengths of **5Ni-am** and **5Ni-bm** calculated by the TD-DFT method[a]

State	Excitation energy, eV/nm (Oscillator strength)	Excitation (Weight [%])
5Ni-am		
4	1.55/800 (0.298)	HOMO → LUMO (96.2)
7	2.03/611 (0.402)	HOMO−2 → LUMO (94.6)
9	2.89/429 (0.131)	HOMO → LUMO+1 (95.9)
13	3.15/393 (0.707)	HOMO−2 → LUMO+1 (43.7), HOMO−3 → LUMO (38.5)
20	3.51/353 (0.430)	HOMO−10 → LUMO (51.6)
5Ni-bm		
4	1.51/820 (0.267)	HOMO → LUMO (95.6)
7	2.02/613 (0.376)	HOMO−2 → LUMO (95.3)
14	3.12/398 (0.753)	HOMO−2 → LUMO+1 (44.2), HOMO−3 → LUMO (23.1)
17	3.30/376 (0.149)	HOMO−5 → LUMO (47.3), HOMO−3 → LUMO (26.7)
22	3.48/356 (0.642)	HOMO−17 → LUMO (34.8)

[a] M062X/6-311G(*d*,*p*) and Wachters–Hay(f) (PCM, CH_2Cl_2) at the optimized structures. The states whose oscillator strengths are less than 0.1 are not included.

para-Me_2N groups were protonated on the N atoms, losing their electron-donating capability. Hence, we conclude that the lowest-energy, HOMO-to-LUMO electronic excitations of **5M** possess a CT character from the donor (tertiary amine) to acceptor (DAP). When the UV/vis/NIR absorption spectra of **5Ni-a** was measured in toluene, the broad NIR band was appreciably blue-shifted (Fig. 3d). The same was true for **5Cu-a**. The observed solvatochromic behavior supported the CT character of the lowest-energy NIR band.

To access the redox properties of TADAP–TAs, we investigated their electrochemical behavior in CH_2Cl_2 by cyclic voltammetry (CV) and differential pulse voltammetry (DPV) with Bu_4NPF_6 as a supporting electrolyte (Table 1). As shown in Fig. 5a, **4Ni-a** exhibited two reversible electrochemical processes at $E_{1/2}$ = –0.69 V and +0.02 V *vs*. ferrocene/ferrocenium couple (Fc/Fc^+), corresponding to the 20π/19π and 19π/18π redox reactions on the DAP ring, respectively. Similar DAP-centered, two separated one-electron redox couples were observed for **4Ni-b** ($E_{1/2}$ = –0.64 V and +0.03 V *vs*. Fc/Fc^+) and **4Cu-a** ($E_{1/2}$ = –0.71 V and –0.01 V *vs*. Fc/Fc^+). In addition to these reversible redox processes, irreversible oxidation processes were observed for all TADAP–TAs at more positive potentials. On the basis of the results of DFT calculations on **5Ni-m**, we considered that the peripheral amine-centered oxidation took place after the generation of the 18π TADAP dications. The anodic peak potential corresponding to the amine oxidation of **5Ni-b** (E_{pa} = *ca*. +1.3 V *vs*. Ag/Ag^+) is comparable to that of an isoelectronic Zn-porphyrin–triphenylamine conjugate (E_{pa} = +1.29 V *vs*. Ag/Ag^+; in CH_2Cl_2, with Bu_4NPF_6) [21] and appreciably shifted to the positive side compared with that of unsubstituted triphenylamine (E_{pa} = +1.20 V *vs*. Ag/Ag^+; in CH_2Cl_2, with Bu_4NPF_6) [22]. These results indicate that the dicationic 18π TADAP substituent had a lower HOMO level than that of triphenylamine [23].

To reveal the electrochemical behavior of **5Ni-b** in more detail, we performed repeat CV scans in the range of –0.47 to +1.03 V *vs*. Fc/Fc^+ (0 to +1.5 V *vs*. Ag/Ag^+) with the use of a freshly polished working electrode. The results are summarized in Fig. 5b. The first anodic scan showed an irreversible peak at E_{pa} = +0.77 V, whereas the first cathodic scan exhibited a new pair of peaks at the more negative potentials. From the second cycle, two reversible redox processes appeared with $E_{1/2}$ values of +0.49 and +0.61 V (*vs*. Fc/Fc^+). The repetitive potential cycling caused the progressive increase in both the anodic and cathodic peak currents of the reversible redox processes including the TADAP-centered 19π/18π couple. The $E_{1/2}$ values after 20 scans (scan rate = 20 mV s^{-1}) were almost identical to those observed for

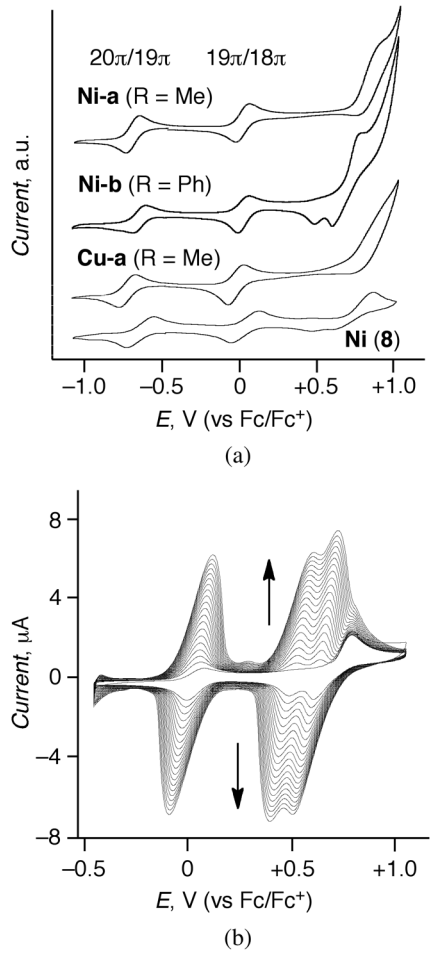

Fig. 5. (a) Cyclic voltammograms of **4Ni-a**, **5Ni-b**, **4Cu-a**, and **8** in CH_2Cl_2 with Bu_4NPF_6 as a supporting electrolyte. Scan rate = 20 mV s^{-1}. (b) Cyclic voltammograms of **5Ni-b** in CH_2Cl_2 with Bu_4NPF_6 as a supporting electrolyte. Repetitive scans (20 times) in the range of –0.47 to +1.03 V *vs*. Fc/Fc^+. Scan rate = 20 mV s^{-1}

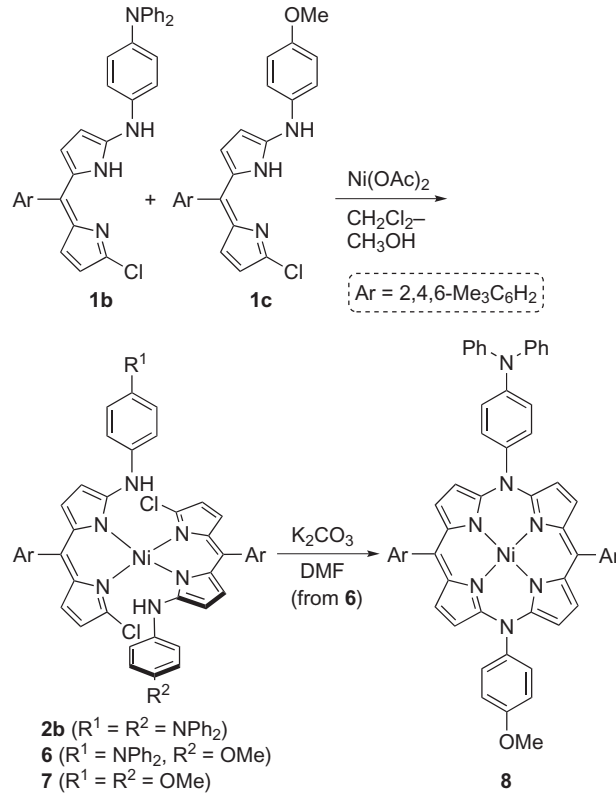

Scheme 3. Synthesis of **8**

the second scan. This kind of electrochemical behavior can be attributed to the formation of a redox-active deposit on the electrode surface. As shown in Fig. 4, the perpendicular orientation between the DAP and *meso*-*N*-phenylene rings in **5Ni-bm** prevents effective overlap of their *p*-orbitals. We thus infer that the TADAP π-spacer in **5Ni-b** cannot contribute to spin delocalization of the ammoniumyl radicals generated at the periphery. It is probable that the reactive ammoniumyl radicals underwent intermolecular coupling on the *N*-phenyl rings to form benzidine-linked TADAP polymers on the electrode surface after the furthest anodic oxidation [24]. Repeated scans of **5Ni-a** and **5Cu-a** did not show either a new pair of redox couples or a progressive increase of the currents indicates that the triphenylamine units in **5Ni-b** played a key role in the electrochemical polymerization. Furthermore, we applied CV measurements to a polymer-coated working electrode, which had been rinsed with CH_2Cl_2 and then placed in a cell filled with a new CH_2Cl_2 solution containing only Bu_4NPF_6. This polymer-coated electrode also showed characteristic cyclic voltammograms comprising four redox couples, which indicated that the redox-active benzidine-linked TADAP polymers were immobilized on the electrode surface. Similar electrochemical polymerization reactions of TAP–triphenylamine conjugates have been reported by Gervaldo and coworkers [25]. When compared with the reported values of their benzidine-linked TAP polymers ($E_{1/2}$ = +0.75 and +0.95 V *vs*. SCE; in CH_2Cl_2, with Bu_4NPF_6) [25], the redox potentials of the present polymer ($E_{1/2}$ = +0.95 and +1.07 V *vs*. SCE) are appreciably shifted to the positive side, if the Fc/Fc^+ couple under the same conditions is referenced to +0.46 V *vs*. SCE [26]. It seems that the dicationic TADAP spacers have a markedly lower HOMO level for the benzidine-linked polymer compared with that of the isoelectronic porphyrin spacers.

To understand the effect of the number of triphenylamine units on the electrochemical behavior of TADAP–TAs, we synthesized new 20π Ni-TADAP–TA **8** bearing one triphenylamine unit (Scheme 3). Treatment of nickel(II) acetate with an equimolar mixture of **1b** and **1c** in CH_2Cl_2–MeOH yielded an unsymmetrical complex **6** together with two kinds of symmetrical complexes **2b** and **7**. These three nickel(II)–bis(dipyrrin) complexes were successfully separated by silica-gel column chromatography, and the isolated **6** was then reacted with

K_2CO_3 in DMF at 110 °C. As expected, the 20π TADAP **8** was obtained as a reddish brown solid and fully characterized by ^1H and ^{13}C NMR spectroscopy and HRMS spectrometry. The ^1H NMR spectrum of **8** in C_6D_6 exhibited four kinds of upfield-shifted pyrrolic β-protons at δ 3.41–4.69 ppm that reflected the paratropic ring-current effects of the antiaromatic DAP π-electron system. The electrochemical behavior of **8** was studied by CV (Fig. 5). In addition to the reversible 20π/19π and 19π/18π redox couples ($E_{1/2}$ = –0.63 and +0.06 V, respectively, *vs*. Fc/Fc^+), an irreversible process was observed at E_{ox} = +0.76 V (*vs*. Fc/Fc^+; not shown here). However, repeat scans did not change the appearance of voltammograms. This result implies that at least two triphenylamine units would be necessary to cause electrochemical polymerization of TADAP–TA [27].

In summary, we prepared the first examples of metal(II) complexes of TADAP–TAs and elucidated their optical, magnetic, and electrochemical properties through the use of spectroscopic and electrochemical techniques and DFT calculations. NMR spectroscopy revealed that the 20π and 18π Ni-TADAP–TAs exhibited antiaromaticity and aromaticity, respectively, in terms of magnetic criterion. EPR spectroscopy of the 19π Ni-TADAP–TA confirmed that the peripherally attached tertiary amine units did not contribute to the electron-spin delocalization of the TADAP radical cations. UV/vis/NIR spectroscopy of all the TADAP–TAs revealed that the peripheral amine units considerably influenced the optical properties of the dicationic 18π TADAP chromophores; they behaved as electron-donor units to provide charge-transfer character to the HOMO-to-LUMO electronic excitations. Furthermore, we revealed that the 18π Ni-TADAP–triphenylamine conjugate was electrochemically oxidized at the amine units to form a polymer film on the electrode surface. The present findings provide a valuable strategy to synthesize redox-active polymer materials composed of DAP and triarylamine units, and further studies on this subject are now in progress.

EXPERIMENTAL

General

All melting points were recorded on a Yazawa micro melting point apparatus and are uncorrected. ^1H NMR and $^{13}C\{^1H\}$ NMR spectra were recorded on an Agilent 700 MHz or 400 MHz spectrometer using $CDCl_3$ or CD_2Cl_2 as a solvent. Chemical shifts are reported as relative values *vs*. tetramethylsilane. High-resolution mass spectra (HRMS) were obtained on a Thermo Fisher Scientific EXACTIVE spectrometer. UV-vis absorption spectra were measured at room temperature on a JASCO V-530 spectrometer. IR (Attenuated Total Reflection; ATR) spectra were obtained on a JASCO FT/IR4600 spectrometer. Chemicals and solvents were of reagent grade quality and used without further purification unless otherwise noted. Thin-layer chromatography was performed with Alt. 5554 DC-Alufolien Kieselgel 60 F254 (Merck), and preparative column chromatography was performed using Silica Gel 60 spherical, neutrality (Nacalai tesque). All reactions were performed under an argon or nitrogen atmosphere. The synthetic procedures and characterization data of new compounds are described below.

Synthesis and Characterization

9-*Arylamino*-1-*chloro*-5-*mesityldipyrrins* (1a,b). Typical procedure: A mixture of 1,9-dichloro-5-mesityldipyrromethene (709 mg, 2.14 mmol), *N*,*N*-dimethyl-1,4-benzenediamine (861 mg, 6.31 mmol), and MeCN (10 mL) was stirred for 17 h at room temperature. After being quenched with water, the aqueous layer was extracted with CH_2Cl_2, and the combined organic extracts were dried over Na_2SO_4 and evaporated under reduced pressure. The residue was then subjected to silica-gel column chromatography (hexane/AcOEt = 5/1). The red fraction (R_f = 0.23; hexane/AcOEt = 5/1) was collected and evaporated to give **1a** as a red oil (850 mg, 92%). Compound **1b** was similarly prepared in 83% yield from 1,9-dichloro-5-mesityldipyrromethene and *N*,*N*-diphenyl-1,4-benzenediamine.

9-(4-*dimethylaminophenyl*)*amino*-1-*chloro*-5-*mesityldipyrrin* (1a): ^1H NMR (400 MHz; $CDCl_3$): δ_H, ppm 2.11 (s, 6H, *ortho*-Me), 2.34 (s, 3H, *para*-Me), 2.96 (s, 6H, NMe), 5.79 (d, 1H, *J* = 3.6 Hz, pyrrole-β), 5.97 (d, 1H, *J* = 3.6 Hz, pyrrole-β), 6.22 (d, 1H, *J* = 4.4 Hz, pyrrole-β), 6.53 (d, 1H, *J* = 4.4 Hz, pyrrole-β), 6.80 (d, 2H, *J* = 8.8 Hz, Ar), 6.90 (s, 2H, Mes-*meta*), 7.43 (d, 2H, *J* = 8.8 Hz, Ar). ^{13}C NMR (100 MHz; $CDCl_3$): δ_C, ppm 19.90, 21.00, 40.88, 108.15, 113.26, 115.14, 118.50, 119.71, 121.65, 126.29, 127.66, 129.42, 132.00, 132.78, 135.31, 136.87, 137.45, 147.32, 162.72, 171.25. HRMS (ESI): *m*/*z* 431.1999 (calcd. for $C_{26}H_{28}ClN_4$: 431.1997, $[M + H]^+$).

9-(4-*diphenylaminophenyl*)*amino*-1-*chloro*-5-*mesityldipyrrin* (1b): Red oil, R_f = 0.23 (hexane/AcOEt = 5/1). ^1H NMR (400 MHz; CD_2Cl_2): δ_H, ppm 2.07 (s, 6H, *ortho*-Me), 2.33 (s, 3H, *para*-Me), 5.76 (d, 1H, *J* = 3.8 Hz, pyrrole-β), 5.96 (d, 1H, *J* = 3.8 Hz, pyrrole-β), 6.29 (d, 1H, *J* = 4.8 Hz, pyrrole-β), 6.53 (d, 1H, *J* = 4.8 Hz, pyrrole-β), 6.92 (s, 2H, Mes-*meta*), 6.98–7.02 (m, 2H, Ph), 7.06–7.13 (m, 4H, Ph), 7.15 (d, 2H, *J* = 9.0 Hz, phenylene), 7.23–7.30 (m, 4H, Ph), 7.54 (d, 2H, *J* = 9.0 Hz, phenylene). ^{13}C NMR (100 MHz; $CDCl_3$): δ_C, ppm 19.95, 21.07, 108.22, 115.63, 118.70, 120.07, 120.71, 122.38, 123.57, 125.42, 127.72, 129.14, 131.78, 132.66, 134.83, 135.58, 137.04, 137.44, 143.06, 146.88, 147.68, 162.22. HRMS (ESI): *m*/*z* 555.2213 (calcd. for $C_{36}H_{32}ClN_4$: 555.2310, $[M + H]^+$).

***Nickel(II)–bis(dipyrrin) complexes* (2a,b).** Typical procedure: A mixture of $Ni(OAc)_2 \cdot 4H_2O$ (121 mg,

0.486 mmol), **1a** (398 mg, 0.924 mmol), CH_2Cl_2 (10 mL), and MeOH (10 mL) was stirred for 1 h at room temperature. The mixture was concentrated under reduced pressure. The solid residue was reprecipitated from CH_2Cl_2–MeOH to give **2a** as a reddish brown solid (343 mg, 81%). Compound **2b** was similarly prepared by the reaction of $Ni(OAc)_2 \cdot 4H_2O$ with **1b**.

2*a*: Yield 85%, mp 127–130 °C, R_f = 0.32 (hexane/AcOEt = 5/1). HRMS (ESI): *m*/*z* 917.3104 (calcd. for $C_{52}H_{53}Cl_2N_8Ni$: 917.3118, $[M + H]^+$).

2*b*: Yield 81%, brown solid, mp 122–124 °C, R_f = 0.60 (hexane/AcOEt = 5/1). HRMS (ESI): *m*/*z* 1165.3726 (calcd. for $C_{72}H_{61}Cl_2N_8Ni$: 1165.3744, $[M + H]^+$).

20π *Ni^{II}TADAP-TA* (3Ni-a,b). Typical procedure: A mixture of **2a** (165 mg, 0.180 mmol), K_2CO_3 (251 mg, 1.81 mmol), and DMF (20 mL) was stirred for 1 h at 110 °C. After being quenched with water, the aqueous layer was extracted with toluene, and the combined organic extracts were washed with brine, dried over Na_2SO_4, and evaporated under reduced pressure. The resulting solid residue was recrystallized from CH_2Cl_2–MeOH to give **3Ni-a** as a reddish brown solid (122 mg, 80%). Compound **3Ni-b** was similarly prepared in 58% yield from **2b**. Compounds **3Ni-a,b** could also be obtained quantitatively by the reaction of **4Ni-a,b** with $CoCp_2$ in THF.

3*Ni-a*: Mp >300 °C, R_f = 0.37 (hexane/AcOEt = 1/1). ^{1}H NMR (400 MHz; C_6D_6): δ_H, ppm 1.96 (s, 6H, *para*-Me), 2.18 (s, 12H, NMe), 2.60 (s, 12H, *ortho*-Me), 3.50 (d, 4H, *J* = 4.4 Hz, pyrrole-β), 4.61 (d, 4H, *J* = 4.4 Hz, pyrrole-β), 6.09 (d, 4H, *J* = 8.8 Hz, Ar), 6.54–6.57 (m, 8H, Ar + Mes-*meta*). HRMS (ESI): *m*/*z* 844.3495 (calcd. for $C_{52}H_{50}N_8Ni$: 844.3506, $[M]^+$). UV-vis (CH_2Cl_2): λ_{max}, nm (log ε) 313 (4.39), 448 (4.86), 534 (4.75).

3*Ni-b*: Reddish brown solid, mp 212–214 °C, R_f = 0.74 (hexane/AcOEt = 5/1). ^{1}H NMR (400MHz; C_6D_6): δ_H, ppm 1.94 (s, 6H, *para*-Me), 2.54 (s, 12H, *ortho*-Me), 3.50 (d, 4H, *J* = 4.4 Hz, pyrrole-β), 4.66 (d, 4H, *J* = 4.4 Hz, pyrrole-β), 6.40 (d, 4H, *J* = 9.0 Hz, phenylene), 6.54 (s, 4H, Mes-*meta*), 6.63 (d, 4H, 9.0 Hz, phenylene), 6.73–6.77 (m, 10H, Ph), 6.86–6.90 (m, 10H, Ph). HRMS (ESI): *m*/*z* 1092.4122 (calcd. for $C_{72}H_{58}N_8Ni$: 1092.4132, $[M]^+$). UV-vis (CH_2Cl_2): λ_{max}, nm (log ε) 305 (4.64), 448 (4.84), 533 (4.74).

19π *Ni^{II}TADAP-TA* (4Ni-a,b). Typical procedure: A mixture of **3Ni-a** (64.8 mg, 0.0766 mmol), $AgPF_6$ (19.6 mg, 0.0775 mmol), and CH_2Cl_2 (10 mL) was stirred for 2 min at room temperature. The mixture was then concentrated under reduced pressure. The residue was subjected to silica-gel column chromatography (CH_2Cl_2/acetone = 30/1). The greenish yellow fraction (R_f = 0.59) was collected and evaporated. The solid residue was reprecipitated from CH_2Cl_2–hexane to give **4Ni-a** as a greenish yellow solid (65.1 mg, 85%). Compound **4Ni-b** was similarly prepared from **3Ni-b**.

4*Ni-a*: Mp >300 °C, R_f = 0.59 (CH_2Cl_2/MeOH = 20/1). HRMS (ESI): *m*/*z* 844.3515 (calcd. for $C_{52}H_{50}N_8Ni$: 844.3506, $[M–PF_6]^+$). IR (ATR): ν, cm^{-1} 835 (PF_6^-). UV-vis-NIR (CH_2Cl_2): λ_{max}, nm (log ε) 312 (4.52), 384 (4.54), 444 (4.67), 858 (4.31).

4*Ni-b*: Greenish yellow solid, mp >300 °C, R_f = 0.59 (CH_2Cl_2/acetone = 20/1). HRMS (ESI): *m*/*z* 1092.4108 (calcd. for $C_{72}H_{58}N_8Ni$: 1092.4132, $[M–PF_6]^+$). IR (ATR): ν, cm^{-1} 833 (PF_6^-). UV-vis-NIR (CH_2Cl_2): λ_{max}, nm (log ε) 311 (4.80), 385 (4.70), 444 (4.86), 861 (4.41).

18π *Ni^{II}TADAP-TA* (5Ni-a,b). Typical procedure: A mixture of **4Ni-a** (29.9 mg, 0.0301 mmol), $AgPF_6$ (8.2 mg, 0.0324 mmol), and CH_2Cl_2 (10 mL) was stirred for 2 min at room temperature and filtrated through a Celite bed. The filtrate was then concentrated under reduced pressure and recrystallized from Et_2O to give **5Ni-a** as a purple solid (29.5 mg, 86%). Compound **5Ni-b** was similarly prepared from **4Ni-b**.

5*Ni-a*: Mp >300 °C, R_f = 0.32 (CH_2Cl_2/acetone = 20/1). ^{1}H NMR (700MHz; CD_2Cl_2): δ_H, ppm 1.84 (s, 12H, *ortho*-Me), 2.56 (s, 6H, *para*-Me), 3.24 (s, 12H, NMe), 7.06 (d, 4H, *J* = 7.7 Hz, Ar), 7.28 (s, 4H, Mes-*meta*), 7.96 (d, 4H, *J* = 7.7 Hz, Ar), 8.51 (d, 4H, *J* = 4.6 Hz, pyrrole-β), 8.67 (d, 4H, *J* = 4.6 Hz, pyrrole-β). HRMS (ESI): *m*/*z* 422.1732 (*z* = 2), 844.3474 (*z* = 1) (calcd. for $C_{52}H_{50}N_8Ni$: 422.1750 (*z* = 2), 844.3506 (*z* = 1), $[M – 2PF_6]^{z+}$). IR (ATR): ν, cm^{-1} 830 (PF_6^-). UV-vis-NIR (CH_2Cl_2): λ_{max}, nm (log ε) 333 (4.55), 397 (4.90), 629 (4.50), 860 (3.35).

5*Ni-b*: Purple solid, mp >300 °C, R_f = 0.49 (CH_2Cl_2/acetone = 20/1). ^{1}H NMR (700MHz; CD_2Cl_2): δ_H, ppm 1.84 (s, 12H, *ortho*-Me), 2.56 (s, 6H, *para*-Me), 7.24–7.27 (m, 4H, Ar), 7.28 (s, 4H, Mes-*meta*), 7.33 (d, 4H, *J* = 8.8 Hz, phenylene), 7.38–7.41 (m, 8H, Ph), 7.44–7.48 (m, 8H, Ph), 7.93 (d, 4H, *J* = 8.8 Hz, phenylene), 8.61 (broad-s, 4H, pyrrole-β), 8.77 (broad-s, 4H, pyrrole-β). HRMS (ESI): *m*/*z* 546.2050 (*z* = 2), 1092.4104 (*z* =1) (calcd. for $C_{72}H_{58}N_8Ni$: 546.2063 (*z* = 2), 1092.4132 (*z* = 1), $[M – 2PF_6]^{z+}$). IR (ATR): ν, cm^{-1} 835 (PF_6^-); UV-vis-NIR (CH_2Cl_2): λ_{max}, nm (log ε) 305 (4.75), 324 (4.76), 400 (5.03), 626 (4.57), 863 (3.49).

19π *Cu^{II}TADAP-TA* (4Cu-a). A mixture of **2a** (131 mg, 0.30 mmol), $Cu(OAc)_2$ (54.7 mg, 0.30 mmol), CH_2Cl_2 (5 mL), and MeOH (5 mL) was stirred for 18 h at room temperature. The mixture was then concentrated under reduced pressure, and the residue was dissolved in CH_2Cl_2 and mixed with an aqueous solution of KPF_6. The resulting mixture was vigorously stirred at room temperature until anion-exchange was almost complete (checked by TLC). The organic phase was separated, dried over Na_2SO_4, and concentrated under reduced presure to leave a solid residue, which was then subjected to silica-gel column chromatography (CH_2Cl_2/MeOH = 20/1). The greenish yellow fraction (R_f = 0.41; CH_2Cl_2/MeOH = 10/1) was collected and evaporated. The solid residue was reprecipitated from CH_2Cl_2–hexane to give **4Cu-a** as a greenish yellow solid (85 mg, 57%). Mp >300 °C. HRMS (ESI): *m*/*z* 849.3439 (calcd. for $C_{52}H_{50}CuN_8$: 849.3449, $[M – PF_6]^+$). IR (ATR): ν, cm^{-1}

832 (PF_6^-). UV-vis-NIR (CH_2Cl_2): λ_{max}, nm (log ε) 315 (4.59), 387 (4.76), 445 (4.88), 867 (4.50).

18π *Cu^{II}TADAP-TA* (**5Cu-a**). A mixture of **4Cu-a** (30.7 mg, 0.0308 mmol), $AgPF_6$ (20.0 mg, 0.0790 mmol), and CH_2Cl_2 (5 mL) was stirred for 2 min at room temperature and filtrated through a Celite bed. The filtrate was then concentrated under reduced pressure and recrystallized from Et_2O to give **5Cu-a** as a purple solid (21.0 mg, 60%). Mp >300 °C. HRMS (ESI): *m*/*z* 424.6712 (*z* = 2), 849.3431 (*z* = 1) (calcd for $C_{52}H_{50}CuN_8$: 424.6722 (*z* = 2), 849.3449 (*z* = 1), $[M-2PF_6]^{z+}$). IR (ATR): ν, cm^{-1} 835 (PF_6^-). UV-vis-NIR (CH_2Cl_2): λ_{max}, nm (log ε) 396 (4.86), 629 (4.72), 870 (3.43).

***Reaction of* 4*Cu-a* with Cp_2Co.** The result is not shown in Scheme 2. A mixture of **4Cu-a** (25.3 mg, 0.0254 mmol), cobaltocene (6.5 mg, 0.035 mmol), and THF (5 mL) was stirred for 2 min at room temperature. The formation of the 20π species was confirmed by UV/vis/NIR absorption spectroscopy (λ_{max} = 447, 523 nm in CH_2Cl_2). However, attempts to isolate the 20π Cu-TADAP–TA in pure form have so far been unsuccessful because the 19π species was readily reproduced during the isolation process.

***Nickel(II)–bis(dipyrrin) complexes* (2b, 6, 7).** A mixture of $Ni(OAc)_2 \cdot 4H_2O$ (91 mg, 0.36 mmol), **1b** (194 mg, 0.349 mmol), **1c** (144 mg, 0.346 mmol), triethylamine (1 mL), CH_2Cl_2 (10 mL), and MeOH (10 mL) was stirred for 30 min at room temperature, and the mixture was concentrated under reduced pressure. The solid residue was then subjected to silica-gel column chromatography (hexane/EtOAc = 10/1) to give three kinds of nickel(II)–bis(dipyrrin) complexes **2b** (82.3 mg, 20%; R_f = 0.72; hexane/EtOAc = 5/1), **6** (120 mg, 34%; R_f = 0.62; hexane/EtOAc = 5/1), and **7** (65.5 mg, 21%; R_f = 0.48; hexane/EtOAc = 5/1).

6: Brown solid, mp 150–152 °C. HRMS (ESI): *m*/*z* 1027.3018 (calcd for $C_{61}H_{53}Cl_2N_7NiO$: 1027.3037, $[M]^+$).

20π *Ni^{II}TADAP-TA* (8). This compound was prepared from **6** in 76% yield according to a similar procedure described in the synthesis of **3Ni-a**. Reddish brown solid, mp 205–208 °C, R_f = 0.46 (hexane/AcOEt = 5/1). ^{1}H NMR (400MHz; C_6D_6): δ_H, ppm 1.98 (s, 6H, *para*-Me), 2.59 (s, 12H, *ortho*-Me), 2.97 (s, 3H, OMe), 3.41 (d, 2H, *J* = 4.9 Hz, pyrrole-β), 3.50 (d, 2H, *J* = 4.9 Hz, pyrrole-β), 4.66–4.69 (m, 4H, pyrrole-β), 6.33 (d, 2H, *J* = 8.4 Hz, phenylene), 6.43 (d, 2H, *J* = 8.4 Hz, phenylene), 6.48 (2H, *J* = 8.4 Hz, phenylene), 6.57 (s, 4H, Mes-*meta*), 6.67 (d, 2H, *J* = 8.4 Hz, phenylene), 6.76–6.82 (m, 6H, Ph), 6.91–6.94 (m, 4H, Ph). ^{13}C NMR (100MHz; C_6D_6): δ_C, ppm 19.66, 21.33, 55.03, 103.96, 116.80, 124.10, 125.16, 125.52, 128.82, 130.01, 130.76, 133.13, 136.93, 147.94, 148.25, 159.74, 162.44. HRMS (ESI): *m*/*z* 955.3485 (calcd. for $C_{61}H_{51}N_7NiO$: 955.3503, $[M]^+$). UV-vis (CH_2Cl_2): λ_{max}, nm (log ε) 308 (4.58), 447 (4.93), 532 (4.83).

Computational Details: The geometries of the model compounds, in which the *meso*-mesityl groups were replaced by phenyl groups, were optimized using the DFT method. The basis sets used were 6-311G(*d*,*p*) basis set [28] for H, C, and N and the Wachters-Hay all electron basis set [29] supplemented with one *f*-function (exponent: 1.29) for Ni. The functional of DFT was the Becke, three-parameter, Lee–Yang–Parr (B3LYP) exchange-correlation functional [30]. We confirmed that the optimized geometries were not in saddle but in stable points. All the calculations were carried out using the Gaussian 09 suite of programs [31].

EPR Measurements: The electron paramagnetic resonance (EPR) spectra of **4Ni-a,b** were measured at room temperature by using a JEOL JES-FA200 spectrometer equipped with an OXFORD ESR900 He-flow cryostat. The sample was prepared as a CH_2Cl_2 solution. After three freeze-pump-thaw cycles, the solution sample in a quartz tube was sealed by frame. Spectral simulation was performed using EasySpin [32], which is a MATLAB toolbox meant for this. The static magnetic field and microwave frequency were measured by Echo Electronics EFM-2000 gauss meter and TakedaRiken TR5212 microwave counter, respectively.

CV and DPV Measurements: Electrochemical measurements were performed at room temperature on a CH Instruments model 650E electrochemical workstation using a glassy carbon or Pt working electrode, a Pt wire counter electrode, and an Ag/Ag^+ [0.01 M $AgNO_3$, 0.1 M Bu_4NPF_6 (MeCN)] reference electrode in a conventional three-electrode cell. The sample solutions were deoxygenated by bubbling with nitrogen gas before the scan. Scan rate was 20 mV s^{-1} unless otherwise noted, and the potentials are reported *vs*. Ag/Ag^+ or ferrocene/ferrocenium (external reference; $E_{1/2}$ = +0.47 V *vs*. Ag/Ag^+). The electrochemical polymerization of **5Ni-b** was conducted under similar conditions with the scan rate of 20 mV s^{-1}. The polymer-coated working electrode was removed from the solution, rinsed with CH_2Cl_2, and then placed in the cell filled with a CH_2Cl_2 solution containing only Bu_4NPF_6.

Acknowledgements

This work was supported by JSPS KAKENHI (Grant Numbers: 18H01961 to YM, 18K05036 to HN).

REFERENCES

1. Kobayashi N. In *The Porphyrin Handbook*, Vol. 2. Kadish KM, Smith KM and Guilard R. (eds). Academic Press: San Diego, CA, 2000; 301–360.
2. Ogata H, Fukuda T, Nakai K, Fujimura Y, Neya S, Stuzhin PA and Kobayashi N. *Eur. J. Inorg. Chem*. 2004; 1621–1629.
3. Mack J and Kobayashi N. *Chem. Rev*. 2011; **111**: 281–321.
4. Matano Y, Shibano T, Nakano H, Kimura Y and Imahori H. *Inorg. Chem.* 2012; **51**: 12879–12890.
5. Matano Y. *Chem. Rev*. 2017; **117**: 3138–3191.

6. Omomo S, Furukawa K, Nakano H and Matano Y. *J. Porphyrins Phthalocyanines* 2015; **19**: 775–785.
7. Omomo S, Maruyama Y, Furukawa K, Furuyama T, Nakano H, Kobayashi N and Matano Y. *Chem. Eur. J.* 2015; **21**: 2003–2010.
8. Abou-Chahine F, Fujii D, Imahori H, Nakano H, Tkachenko NV, Matano Y and Lemmetyinen H. *J. Phys. Chem. B* 2015; **119**: 7328–7337.
9. Kawamata M, Sugai T, Minoura M, Maruyama Y, Furukawa K, Holstrom C, Nemykin VN, Nakano H and Matano Y. *Chem. Asian J.* 2017; **12**: 816–821.
10. Omomo S, Tsuji Y, Sugiura K, Higashino T, Nakano H, Imahori H and Matano Y. *ChemPlusChem* 2017; **82**: 695–704.
11. Omomo S, Sugai T, Minoura M, Nakano H and Matano Y. *Angew. Chem. Int. Ed.* 2018; **57**: 3797–3800.
12. Omomo S, Fukuda R, Miura T, Murakami T, Ikoma T and Matano Y. *ChemPlusChem* 2019; **84**: 740–745.
13. Yamaji A, Hiroto S, Shin JY and Shinokubo H. *Chem. Commun*. 2013; **49**: 5064–5066.
14. Longevial JF, Yamaji A, Aggad D, Kim G, Chia WX, Nishimura T, Miyake Y, Clément S, Oh J, Daurat M, Nguyen C, Kim D, Gary-Bobo M, Richeter S and Shinokubo H. *Chem. Commun.* 2018; **54**: 13829–13832.
15. Satoh T, Minoura M, Nakano H, Furukawa K and Matano Y. *Angew. Chem. Int. Ed.* 2016; **55**: 2235–2238.
16. Sudoh K, Satoh T, Amaya T, Furukawa K, Minoura M, Nakano H and Matano Y. *Chem. Eur. J.* 2017; **23**: 16364–16373.
17. Sudoh K, Hatakeyama T, Furukawa K, Nakano H and Matano Y. *J. Porphyrins Phthalocyanines* 2018; **22**: 542–551.
18. Sudoh K, Furukawa K, Nakano H, Shimizu S and Matano Y. *Heteroatom Chem.* 2018; **29**: e21456.
19. Mutoh M, Sudoh K, Furukawa K, Minoura M, Nakano H and Matano Y. *Asian J. Org. Chem.* 2019; **8**: 352–355.
20. Horie M, Hayashi Y, Yamaguchi S and Shinokubo H. *Chem. Eur. J*. 2012; **18**: 5919–5923.
21. Huang CY, Hsu CY, Yang LY, Lee CJ, Yang TF, Hsu CC, Ke CH and Su YO. *Eur. J. Inorg. Chem*. 2012; 1038–1047.
22. Cheng HC, Chiu KY, Lu CC, Chen CC, Lee YW, Yang TF, Kuo MY, Chen PPY and Su YO. *J. Phys. Chem. A* 2015; **119**: 1933–1942.
23. The observed difference cannot be attributed to the electronic effect of the central metals because Pauling electronegativity values of Ni and Zn are 1.91 and 1.65, respectively.
24. The electrochemical oxidation of triphenylamine causes the generation of a reactive radical cation, which typically undergoes dimerization to *N*,*N*,*N*′,*N*′-tetraphenylbenzidine as a result of oxidative coupling at the *para* positions. For example, see: Yurchenko O, Freytag D, zur Borg L, Zentel R, Heinze J and Ludwigs S. *J. Phys. Chem. B* 2012; **116**: 30–39.
25. Gervaldo M, Funes M, Durantini J, Fernandez L, Fungo F and Otero L. *Electrochim. Acta* 2010; **55**: 1948–1957.
26. Connelly NG and Geiger WE. *Chem. Rev.* 1996; **96**: 877–910.
27. For other examples of electrochemical polymerization of TAPs bearing multiple 4-(*N*,*N*-diphenylamino)pheyl groups at the *meso* positions, see: (a) Funes MD, Caminos DA, Alvarez MG, Fungo F, Otero LA and Durantini EN. *Environ. Sci. Technol.* 2009; **43**: 902–908. (b) Durantini J, Morales GM, Santo M, Funes M, Durantini EN, Fungo F, Dittrich T, Otero L and Gervaldo M. *Org. Electron.* 2012; **13**: 604–614. (c) Noworyta K, Kutner W, Wijesinghe CA, Srour SG and D'Souza F. *Anal. Chem*. 2012; **84**: 2154–2163.
28. Krishnan R, Binkley JS, Seeger R and Pople JA. *J. Chem. Phys.* 1980; **72**: 650–654.
29. (a) Wachters AJH. *J. Chem. Phys*. 1970; **52**: 1033–1036. (b) Hay PJ. *J. Chem. Phys*. 1977; **66**: 4377–4384. (c) Raghavachari K and Trucks GW. *J. Chem. Phys.* 1989; **91**: 1062–1065.
30. (a) Becke AD. *J. Chem. Phys.* 1993; **98**: 5648–5652. (b) Lee C, Yang W and Parr RG. *Phys. Rev. B* 1988; **37**: 785–789.
31. Frisch MJ, Trucks GW, Schlegel HB, Scuseria GE, Robb MA, Cheeseman JR, Scalmani G, Barone V, Mennucci B, Petersson GA, Nakatsuji H, Caricato M, Li X, Hratchian HP, Izmaylov AF, Bloino J, Zheng G, Sonnenberg JL, Hada M, Ehara M, Toyota K, Fukuda R, Hasegawa J, Ishida M, Nakajima T, Honda Y, Kitao O, Nakai H, Vreven T, Montgomery, Jr. JA, Peralta JE, Ogliaro F, Bearpark M, Heyd JJ, Brothers E, Kudin KN, Staroverov VN, Keith T, Kobayashi R, Normand J, Raghavachari K, Rendell A, Burant JC, Iyengar SS, Tomasi J, Cossi M, Rega N, Millam JM, Klene M, Knox JE, Cross JB, Bakken V, Adamo C, Jaramillo J, Gomperts R, Stratmann RE, Yazyev O, Austin AJ, Cammi R, Pomelli C, Ochterski JW, Martin RL, Morokuma K, Zakrzewski VG, Voth GA, Salvador P, Dannenberg JJ, Dapprich S, Daniels AD, Farkas O, Foresman JB, Ortiz JV, Cioslowski J and Fox DJ. *Gaussian 09, Revision B.01*; Gaussian, Inc., Wallingford CT, **2010**.
32. Stoll S and Schweiger A. *J. Magn. Reson*. 2006; **178**: 42–55.